Journal of Energy Chemistry 62 (2021) 477–484

Contents lists available at ScienceDirect

Journal of Energy Chemistry

journal homepage: www.elsevier.com/locate/jechem

http://www.journals.elsevier.com/journal-of-energy-chemistry/

Circumventing chemo-mechanical failure of Sn foil battery anode by grain refinement and elaborate porosity design

Shuibin Tu [a,b], Xin Ai [c], Xiancheng Wang [b], Siwei Gui [c], Zhao Cai [b], Renming Zhan [b], Yuchen Tan [b], Weiwei Liu [b], Hui Yang [c,*], Chenhui Li [a,*], Yongming Sun [b,*]

[a] State Key Laboratory of Material Processing and Die & Mould Technology, School of Materials Science and Engineering, Huazhong University of Science and Technology, Wuhan 430074, Hubei, China
[b] Wuhan National Laboratory for Optoelectronics and School of Optical and Electronic Information, Huazhong University of Science and Technology, Wuhan 430074, Hubei, China
[c] Department of Mechanics, School of Aerospace Engineering, Huazhong University of Science and Technology, Wuhan 430074, Hubei, China

A R T I C L E   I N F O

Article history:
Received 15 February 2021
Revised 25 March 2021
Accepted 25 March 2021
Available online 9 April 2021

Keywords:
Sn foil anode
3D interconnected porous structure
Grain refinement
Uniform alloying/dealloying reaction
Chemo-mechanical failure

A B S T R A C T

Tin (Sn) metal foil is a promising anode for next-generation high-energy–density lithium-ion batteries (LIBs) due to its high capacity and easy processibility. However, the pristine Sn foil anode suffers nonuniform alloying/dealloying reaction with lithium (Li) and huge volume variation, leading to electrode pulverization and inferior electrochemical performance. Herein, we proposed that reduced grain size and elaborate porosity design of Sn foil can circumvent the nonuniform alloy reaction and buffer the volume change during the lithiation/delithiation cycling. Experimentally, we designed a three-dimensional interconnected porous Sn (3DIP-Sn) foil by a facile chemical alloying/dealloying approach, which showed improved electrochemical performance. The enhanced structure stability of the as-fabricated 3DIP-Sn foil was verified by chemo-mechanical simulations and experimental investigation. As expected, the 3DIP-Sn foil anode revealed a long cycle lifespan of 4400 h at 0.5 mA cm^{-2} and 1 mAh cm^{-2} in Sn||Li half cells. A 3DIP-Sn||$LiFePO_4$ full cell with $LiFePO_4$ loading of 7.1 mg cm^{-2} exhibited stable cycling for 500 cycles with 80% capacity retention at 70 mA g^{-1}. Pairing with high-loading commercial $LiNi_{0.6}Co_{0.2}Mn_{0.2}O_2$ (NCM622, 18.4 mg cm^{-2}) cathode, a 3DIP-Sn||NCM622 full cell delivered a high reversible capacity of 3.2 mAh cm^{-2}. These results demonstrated the important role of regulating the uniform alloying/dealloying reaction and circumventing the localized strain/stress in improving the electrochemical performance of Sn foil anodes for advanced LIBs.

1. Introduction

Rechargeable lithium-ion batteries (LIBs) dominate the market of portable electronics and electric vehicles, owing to their advantages of high energy density, long cycle life, and slow self-discharge rate [1–5]. To meet the ever-growing market demands, tremendous efforts have been devoted to improving the energy density of LIBs by exploring high-capacity alloy-type anodes (e.g., Si, Sn, and Ge) to replace the traditional intercalation-type graphite anode with limited capacity (372 mAh g^{-1}, 818 mAh cm^{-3}) [6–12]. Among the alloy-type anodes, Sn metal possesses good electrical conductivity (9.1×10^6 S m^{-1}), high lithium (Li) storage capacity (990 mAh g^{-1}, 7254 mAh cm^{-3}), and low cost [13,14], and thus is a promising anode for next-generation high-energy-density-LIBs. However, Sn-based anodes suffer from drastic volume changes (up to 260% for full lithiation from Sn to $Li_{4.4}Sn$) and stress during the charge/discharge processes, resulting in the pulverization of the materials and even peeling off from the current collector, and thus rapid capacity degradation [15,16]. Till now, several successful strategies have been developed to address the above issues at the particle level, including preparing Sn nanoparticles [17], embedding Sn nanoparticles into carbon matrix [10,11,18], and designing Sn-based alloy nanoparticles [19–21]. Although the specific capacity and cycling stability have been improved, the fabrication of these Sn nanostructures is complicated, and these electrodes generally present a low tap density and take in a high amount of electrolyte during the cell fabrication, which severely reduces the overall energy density of LIBs.

In contrast to particle-based Sn metal electrodes, Sn metal foil has excellent processability and good volumetric capacity, and

---

* Corresponding authors.

E-mail addresses: huiyang2017@hust.edu.cn (H. Yang), lch@hust.edu.cn (C. Li), yongmingsun@hust.edu.cn (Y. Sun).

https://doi.org/10.1016/j.jechem.2021.03.053

does not need to involve the regular electrode fabrication process including slurry coating, electrode baking and calendaring before battery assembly, which is desirable for a practical battery anode [22–24]. To realize an applicative Sn foil electrode, the following challenges should be addressed regarding to the chemo-mechanical stability: (i) The completely compact structure of the foil electrode cannot endure volume change and mitigate stress during the lithiation/delithiation processes of Sn, which easily causes the fast pulverization and failure of the foil electrode compared to the particle-based electrodes with certain porosity. (ii) Sn foil electrode often shows too less accessible surface area to liquid electrolyte and inferior electrolyte wettability compared with the particle-based porous electrodes, which leads to a severe local alloying reaction and large deformation nonhomogeneity; (iii) due to the higher Li diffusivity at the grain boundaries (GBs) than that in the bulk [25–27], electrochemical reaction would take place preferentially at the GBs in metal foil, resulting in the further strain/stress localization and subsequent pulverization of the foil electrode during the Li lithiation/delithiation processes. Although previous study indicated that the introduction of Ag and Cu components into Sn foil could refine the grain size of Sn metal [28], one still has to address the above-mentioned chemo-mechanical concerns simultaneously, which is significantly essential for the development of high-capacity, failure-resistant, and long-cycle-life Sn based electrodes for the next-generation LIBs.

Herein, we explored a facile chemical alloying/dealloying approach to fabricate a three-dimensional interconnected porous Sn (3DIP-Sn) foil through spontaneous reaction between Li metal and Sn foil to form a Li-Sn alloy and its subsequent reduction to metallic Sn in solution. The as-formed 3DIP-Sn layer possesses thickness of ~ 25 μm, and average nanopore size and porosity of ~ 300 nm and 58.7%, respectively. Such 3DIP-Sn foil can effectively refine grain size, eliminate the effect of GBs, improve electrolyte wettability, and buffer volume change, thereby homogenizing the alloying/dealloying reaction and mitigating local strain/stress during the cycling of Sn foil, realizing a highly reversible battery anode. As expected, the 3DIP-Sn foil electrode exhibited a prolonged cycle lifespan of 4400 h at 0.5 mA cm^{-2} and 1 mAh cm^{-2} in Sn||Li half cells. When paired with a commercial $LiFePO_4$ cathode (7.1 mg cm^{-2}), the full cell sustained cycling for 500 cycles with 80% capacity retention at 70 mA g^{-1}. Moreover, a high reversible capacity of 3.2 mAh cm^{-2} was achieved in 3DIP-Sn foil|| NCM622 full cells with a high cathode mass loading of 18.4 mg cm^{-2}.

2. Results and discussion

Fig. 1(a and b) shows the schematic illustration of the electrochemical lithiation processes of Sn foils with different structures. Due to the GB effects, the pristine Sn foil with large-sized grains undergoes non-uniform lithiation during the electrochemical reaction, resulting in huge localized volume expansion and stress inside the foil, accompanied by cracks and the exposure of fresh active regions. Such behavior leads to the continuous extension of the lithiation reaction into the interior of the Sn foil, which eventually pulverizes the foil. Therefore, mitigating the problems caused by GBs and volume expansion simultaneously is the key to achieve a highly stable Sn foil anode. We believe that the ideal Sn foil anode should possess the structural characteristics of refined grain size and appropriate porosity simultaneously to ensure the desired electrochemical reversibility of the electrode, as, on one hand, the grain refinement can improve the homogeneity of lithiation reaction and, on the other hand, the porous structures will help to buffer the Li insertion induced volume change and stress [29] (Fig. 1b). To demonstrate this concept, chemo-mechanical simulations were conducted by coupling lithiation/delithiation kinetics with elasto-plastic large deformation to reveal the effects of grain size (related to the density of GBs) and pores on the lithiation behavior of Sn foils [30]. Fig. 1(c and d) shows the simulated time series snapshots of Li and effective stress (von Mises stress) distributions in Sn foils, respectively. As shown in Fig. 1(c), the blue color indicates the unlithiated phase (c = 0), while the red represents the fully lithiated phase (c = 1). The transition from blue to red denotes the lithiation/delithiation reaction front [30,31]. The corresponding movie (Movie S1) was provided in Supporting Information. Assuming the perfect contact between the top surface of Sn foils and electrolyte, Li flowed into the foils along the thickness direction. Due to the much higher Li diffusivity in the GB region than that in the bulk, Li preferred to migrate along GBs first, causing non-uniform lithiation. For the Sn foil with large-sized grains, the non-uniform lithiation was so severe that cracks nucleated and propagated along GBs. However, with the decrease of grain size, the density of GBs increased, generating a more uniform lithiation pattern in the small-grain Sn foil. Such promoted lithiation homogeneity contributed to a much tougher behavior of small-grain Sn foil than that of large-grain Sn foil, even though damage still occurred at certain GBs inside the foil indicated by the relaxation of local stress in Fig. 1(d). Moreover, with the introduction of randomly distributed pores inside the small-grain Sn foil, the damage at the grain boundaries can even be avoided with the same Li loading.

Inspired by the above analyses and results, we designed a 3DIP-Sn foil using a facile chemical alloying/dealloying method through spontaneous reaction between Li metal and Sn foil to form a Li-Sn alloy at room temperature and subsequent reduction to metallic Sn in solution. As illustrated in Fig. 2(a), a Sn foil and a Li foil were firstly stacked together and calendared by a roller in a glove box. The closely-contact Li and Sn foils were subsequently treated at 100 °C for 2 h to produce a Li/Li_xSn/Sn hybrid. After the exfoliation of the top Li foil layer, the Li_xSn/Sn composite foil was then immersed into ethanol (with 5 wt% water) for 12 h, leading to the generation of a 3DIP-Sn foil featured with an interconnected 3D activated nanoporous Sn layer on a dense Sn layer, the latter of which could serve as the current collector of the electrode. As shown in Fig. 2(b), the pristine Sn foil showed a smooth surface with the average grain size of ~ 83 μm (Fig. 2c and d). After mechanical rolling and heating treatment, the color of the Sn foil turned from silvery white to dark gray (Fig. S1a and b), suggesting the reaction between the metallic Sn and Li. X-ray diffraction (XRD) pattern indicated that the product of alloying reaction between Li and Sn was $Li_{13}Sn_5$ (Fig. S2). According to the result of electrochemical Li extraction measurement in half cells, the overall Li involved in $Li_{13}Sn_5$ was 3.05 mAh cm^{-2} (Fig. S3), implying that the as-prepared 3DIP-Sn foil anode could accommodate 3.05 mAh cm^{-2} of active Li. After washing with ethanol, the obtained 3DIP-Sn foil showed an interconnected nanoporous surface layer with the average pore size of ~ 300 nm (Fig. 2e). The thickness of 3DIP layer was ~ 25 μm (Fig. 2f), which can be adjusted by using different heating temperature for alloying reaction (Fig. S4). The high-angle annular dark field detector (HADDF) image (Fig. 2g) further revealed that the grain size of the 3D interconnected porous layer was about 300–500 nm, indicating the much-refined grain size after structure reconstruction of the Sn foil. In addition, the XRD pattern in Fig. S5 manifested the pure Sn phase of the 3DIP-Sn foil, demonstrating the successful chemical dealloying reaction of $Li_{13}Sn_5$ intermediate. With the elimination of Li, the color of the 3DIP-Sn foil finally changed into grey (Fig. S1c). As shown in Fig. S6, the as-prepared 3DIP-Sn foil could be folded or twisted without any fracture, indicating the excellent connection of the

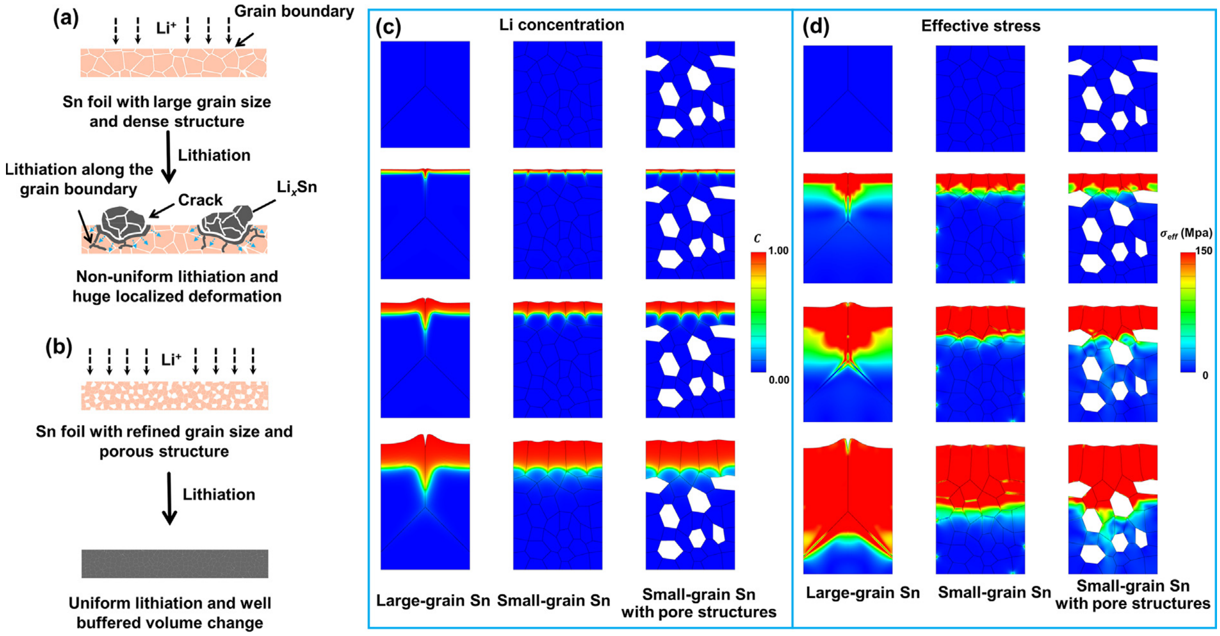

Fig. 1. (a and b) Schematic illustrations of the electrochemical lithiation processes of Sn foils with different structures. Chemo-mechanical simulated time series snapshots of (c) Li and (d) effective stress distributions in Sn foils with large-sized grain, small-sized grain, and small-sized grain and porous structures, respectively.

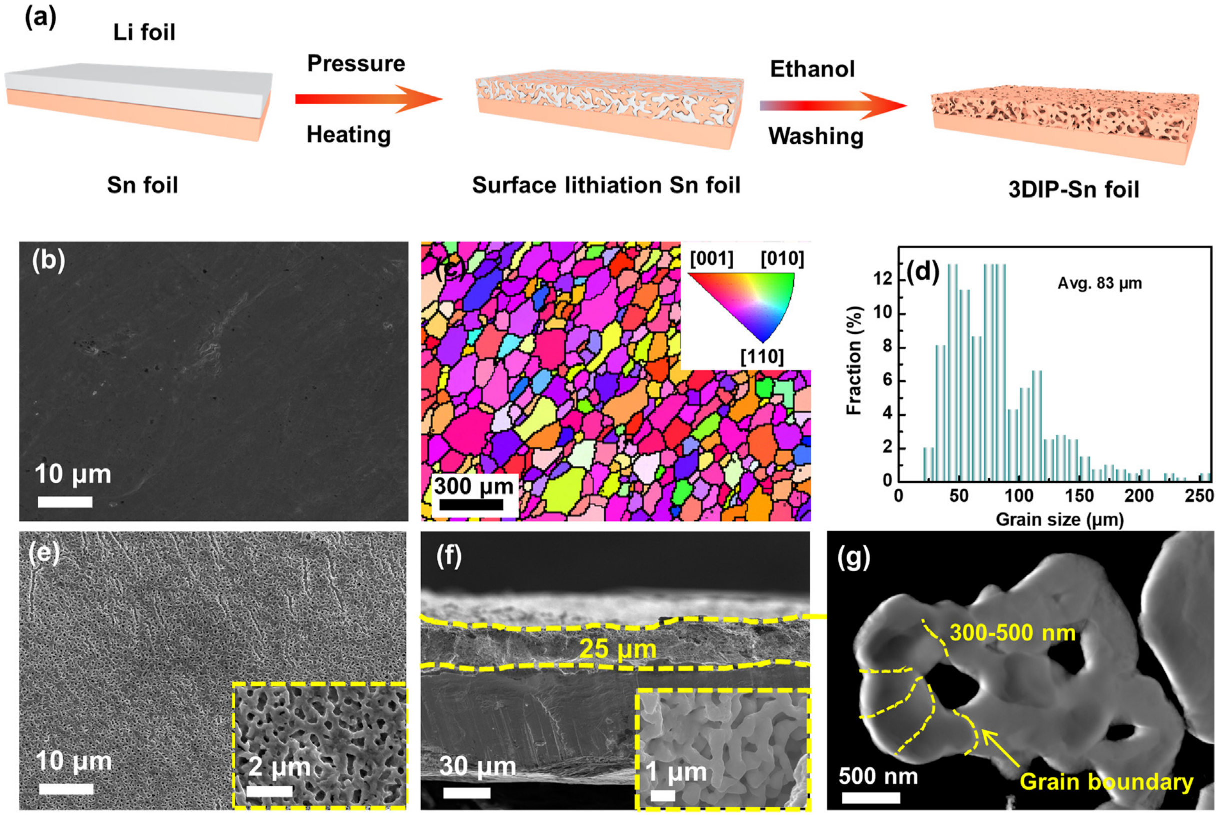

Fig. 2. (a) Schematic illustration of the fabrication process of the 3DIP-Sn foil. (b) Top-view SEM image, (c) the electron-backscatter diffraction (EBSD) inverse pole figure map, and (d) the grain size distribution of the pristine Sn foil. (e) Top-view, (f) cross-section SEM, and (g) HAADF images of the 3DIP-Sn foil. The insets in (e and f) showed the enlarged SEM images for the 3DIP-Sn foil.

3D interconnection porous layer with the bottom compact current collector and thus the enhanced mechanical stability of the active material – current collector integrated structure.

To investigate the electro-chemo-mechanical behaviors of the 3DIP-Sn electrode, electrochemical lithiation measurement with the combination of structure investigation was carried out. As

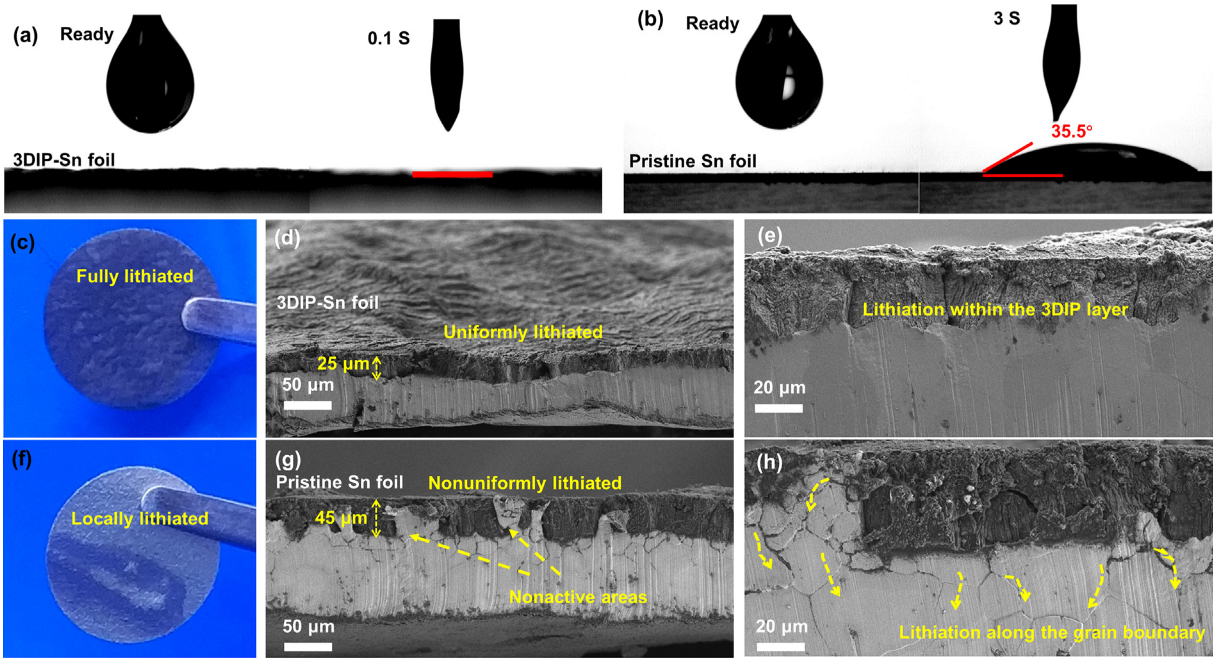

Fig. 3. Contact angle measurements for the electrolyte on the surfaces of (a) 3DIP-Sn and (b) pristine Sn foils, respectively. The digital images of (c) 3DIP-Sn and (f) pristine Sn foil anodes after electrochemical lithiation at 3 mAh cm^{-2} at 1 mA cm^{-2}. Cross-section SEM images of (d and e) 3DIP-Sn and (g and h) pristine Sn foil electrodes after electrochemical lithiation.

shown in Fig. 3(a and b), the electrolyte droplet maintained a large contact angle of 35.5° on the surface of the pristine Sn foil, suggesting inferior wettability, while the instantaneous spread of the droplet on the surface of the 3DIP-Sn foil (0.1 s, contact angle of nearly 0°) led to the thoroughly wetting of the electrode. Such significantly improved electrolyte wettability of the 3DIP-Sn foil can be attributed to the three-dimensional interconnected porous structure of the foil, which can enlarge the effective electrochemical contact area and promote the uniform lithiation/delithiation reaction. As lithiated with a fixed areal capacity of 3 mAh cm^{-2} at 1 mA cm^{-2} in a 3DIP-Sn||Li half-cell, the 3DIP-Sn foil electrode showed homogeneous alloying reaction to produce $Li_{13}Sn_5$ (Fig. S7) with its color changed completely from the initial light gray to dark gray (Fig. 3c). The SEM images in Fig. 3(d and e) revealed that the improved electrolyte wettability and the refined grain size (increased GB density) together can finally lead to the uniform lithiation behavior in the 3DIP-Sn foil. After full lithiation, the thickness of the active layer was still maintained around 25 μm with no obvious volume expansion observed, indicating that the lithiation induced volume change was effectively buffered by the nanoporous structure in the active layer. Thus, no cracks showed up in the active layer or the current collector layer of the 3DIP-Sn foil, demonstrating the well-maintained structure integrity. In contrast, the alloying reaction in the pristine Sn foil was inhomogeneous under the same test condition, with only part of the Sn foil got lithiated (Fig. 3f). As revealed by the XRD pattern in Fig. S7, the lithiation product consisted of mixed phases of Li_7Sn_2 and $Li_{13}Sn_5$, suggesting the nonuniform electrochemical lithiation reaction in the pristine Sn foil. The cross-section SEM images of the lithiated pristine Sn foil (Fig. 3g and h) showed the thickness of the lithiated phase in certain region reached up to ~ 45 μm, while at some locations the thickness was negligible. In addition, the magnified image (Fig. 3h) clearly revealed that Li flowed into the foil primarily along GBs first. Such nonuniform lithiation behavior would certainly generate huge localized deformation and stress that in turn lead to the more severely nonuniform reaction due to the chemo-mechanical coupling effect. Impressively, cracks with the size larger than 10 μm were observed in the lithiated pristine Sn foil along GBs due to the stress concentration caused by the nonuniform lithiation. With further lithiation, the propagation of the cracks would finally lead to the pulverization of the pristine Sn foil electrode. The comparison between the pristine Sn and the 3DIP-Sn foil electrodes evidently revealed the distinct advantages of the 3DIP-Sn foil toward chemo-mechanical failure resistant electrode, including: (i) The nanoporous structure can alleviate the overall electrode volume variation during the charge/discharge processes; (ii) the improved electrolyte wettability can homogenize the electrochemical reaction and eliminate the localized deformation/stress; (iii) the grain refinement helps to mitigate the GB effects and further homogenize the alloying/dealloying reaction of Sn.

The electrochemical performance of the pristine Sn and 3DIP-Sn foil electrodes in the coin-type half cells at various current densities with Li foil as the counter electrode was presented here. As shown in Fig. 4(a and b) and S8, the pristine Sn foil anode delivered a cycle lifespan for less than 1000 h at a current density of 0.5 mA cm^{-2} with a capacity of 1.0 mAh cm^{-2}. The short cycle life could be ascribed to the uneven alloying/dealloying reaction and drastic volume variation during the electrochemical cycling. In contrast, the 3DIP-Sn foil electrode presented a much longer cycle lifespan of 4400 h under the same test condition due to the uniform electrochemical alloying/dealloying processes and effective strain/stress mitigation in the porous structure. When the current density increased to 2 mA cm^{-2}, the 3DIP-Sn foil still exhibited stable cycling for over 250 h, significantly longer than that of the pristine Sn foil (~80 h). The comparison of the potential hysteresis of both electrodes cycled at 0.5 mA cm^{-2} and 1 mAh cm^{-2} (Fig. 4c) further showed that the polarization voltage of the pristine Sn foil electrode increased gradually from 0.16 to 0.4 V within 1024 h (i.e., the 256th cycle), while the 3DIP-Sn foil electrode displayed a much lower and more stable polarization voltage of 0.12 V after 4400 h (i.e., the 1100th cycle). Large voltage polarization of pristine Sn foil may arise from its inferior wettability and low accessible surface to the electrolyte, and large GBs.

Fig. 4(d) and S9 show the voltage profiles of the 3DIP-Sn foil and pristine Sn foil electrodes at 0.5 mA cm^{-2} and 1 mAh cm^{-2}, respectively. The 3DIP-Sn foil electrode exhibited a stable lithiation volt-

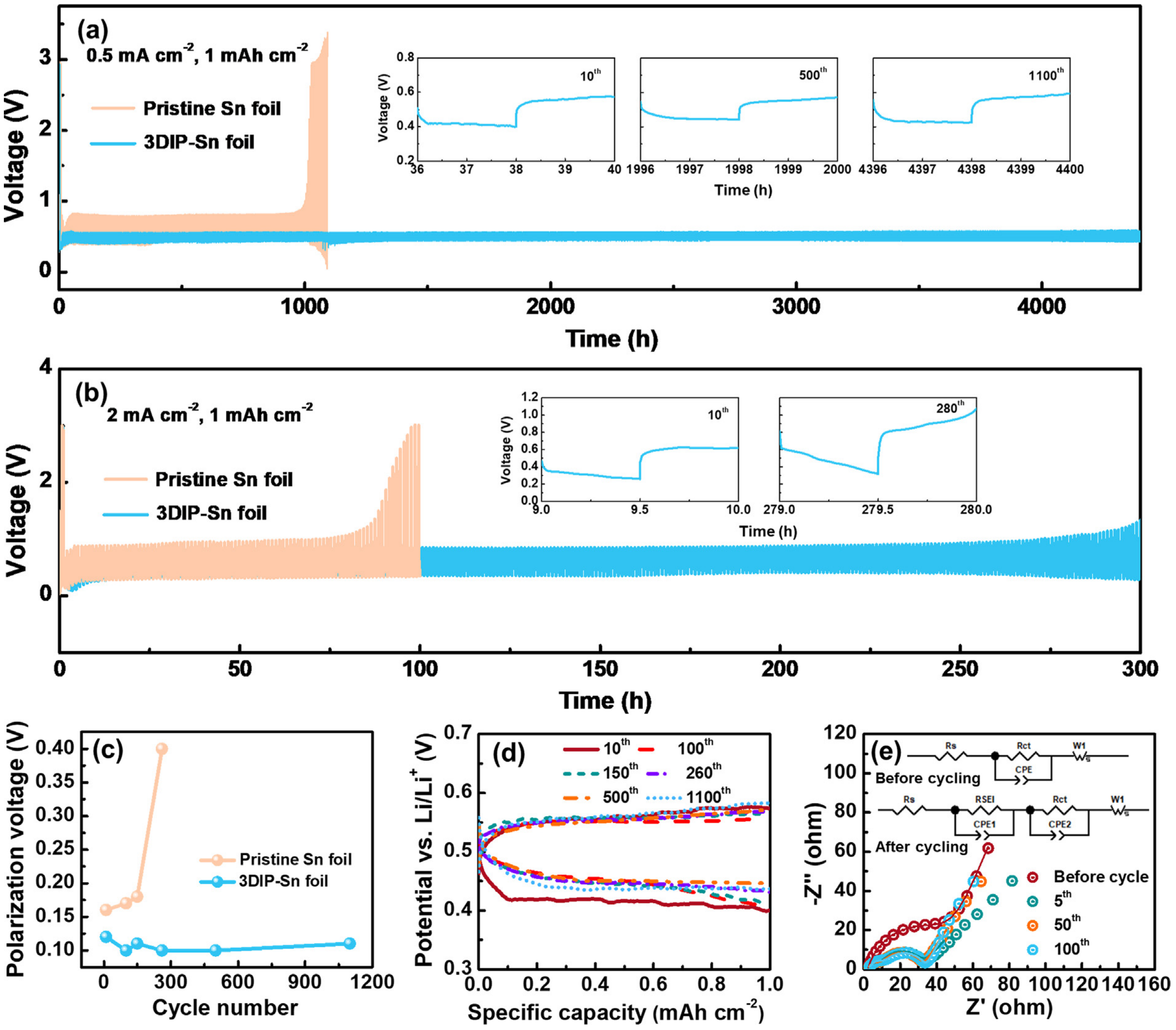

Fig. 4. Galvanostatic cycling performance of the pristine Sn and 3DIP-Sn foil electrodes in half cells using Li metal as the counter electrode at (a) 0.5 mA cm^{-2} and 1 mAh cm^{-2} and (b) 0.5 mA cm^{-2} and 1 mAh cm^{-2}. (c) Potential hysteresis of the pristine Sn and 3DIP-Sn foil electrodes at different cycles at 0.5 mA cm^{-2} and 1 mAh cm^{-2}. (d) Voltage profiles of the 3DIP-Sn foil electrode at different cycles at 0.5 mA cm^{-2} and 1 mAh cm^{-2}. (e) EIS spectra of the 3DIP-Sn foil electrode after different cycles. The inset shows the corresponding fitted equivalent circuit diagrams.

age plateau at 0.42 V on cycling, indicating the uniform alloying reaction. However, the different potential curves of the pristine Sn foil electrode displayed continuously varying voltage plateaus during cycling. Such unstable voltage plateaus indicated the different extents of electrochemical reaction and utilization of active Sn, further demonstrating the nonuniform electrochemical reaction and unstable electrode structure of the pristine Sn foil electrode.

As shown by the SEM images of the two electrodes after 100 cycles at 2 mA cm^{-2} and 1.0 mAh cm^{-2} (Fig. S11), severe pulverization was observed for the pristine Sn foil electrode, while the structure of the 3DIP-Sn electrode remained intact and showed only ~ 28% volume expansion after 100 cycles (with thickness increase from 25 to 32 μm), similar to the graphite electrode. The improved electrochemical stability of the 3DIP-Sn foil was further confirmed by the results of electrochemical impedance spectroscopy (EIS) measurements, the Nyquist plots of the 3DIP-Sn and pristine Sn foil anodes and corresponding equivalent circuit are depicted in Fig. 4(e) and S12. The fresh anodes show one semicircle at the high-frequency region and a straight line in the low-frequency region for both electrodes, corresponding to the charge transfer resistance (R_{ct}) and diffusion of lithium ions. Before cycling, R_{ct} of the 3DIP-Sn foil electrode (42 Ω) was much lower than that of the pristine Sn foil electrode (310 Ω). After 5 cycles, the two semicircles appeared the high-frequency region, representing the resistance of the SEI film (R_{SEI}) and R_{ct}, respectively. The R_{ct} of the 3DIP-Sn foil electrode decreased to 21 Ω and then kept stable along with cycling, suggesting good interface stability. As to the pristine Sn foil anode, although the R_{ct} decreased to 143 Ω and 24 Ω at the 5th and 50th cycles, respectively, slightly increased to 28 Ω at the 100th cycle (Fig. S12). Besides, 3DIP-Sn foil displayed much smaller and more stable R_{SEI} (7 Ω and 8 Ω at 5th and 100th cycles, respectively) in comparison to pristine Sn foil (98 Ω and 47 Ω at 5th and 100th cycles, respectively), further indicating that the advancement of the 3DIP-Sn foil electrode. Such unstable performance, increased R_{ct} and large R_{SEI} after electrochemical activation for the pristine Sn foil, in turn, demonstrated the much-improved structural stability and electrochemical performance of the 3DIP-Sn foil electrode.

To further understand the effect of 3D nanoporous structure on the lithiation/delithiation behaviors of Sn foil, chemo-mechanical simulations were conducted herein. For comparison, pristine Sn foil was also studied. Fig. 5 shows the simulated time series snap-

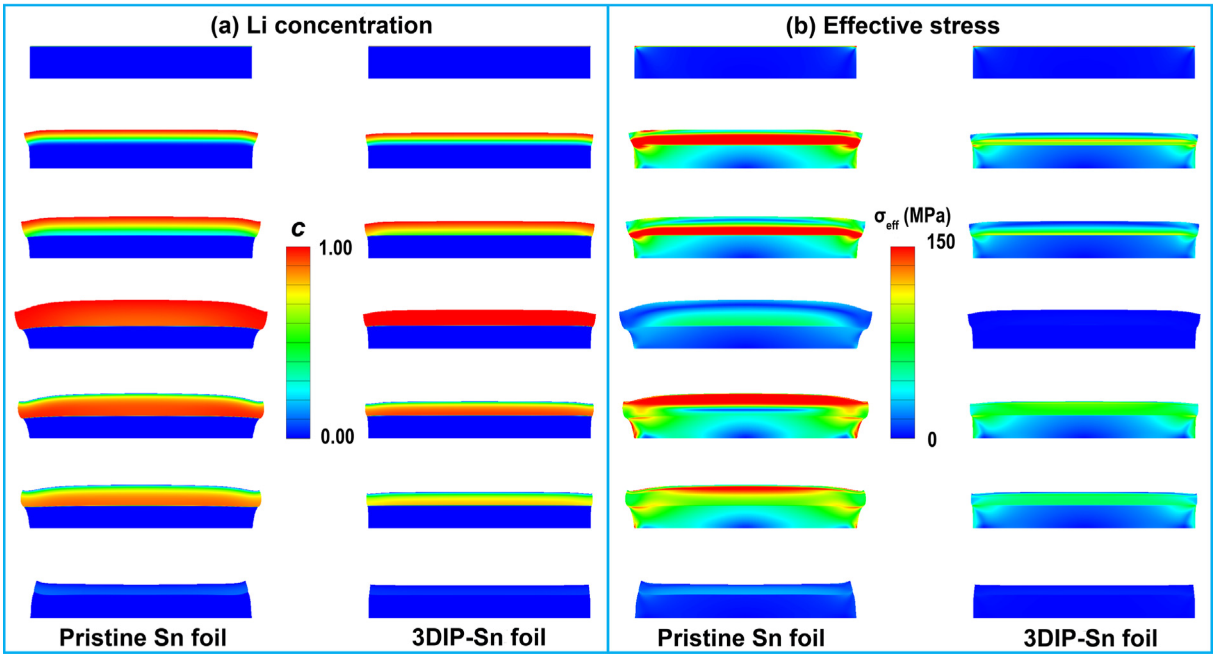

Fig. 5. Chemo-mechanical simulated time series snapshots of (a) Li and (b) effective stress distributions on the cross-section of circular-shaped pristine Sn and 3DIP-Sn foils during lithiation/delithiation processes, respectively.

shots of (a) Li and (b) effective stress distributions on the cross section of circular-shaped pristine Sn foil and 3DIP-Sn foil, respectively. The corresponding movie (Movie S2) was provided in Supporting Information. As shown in Fig. 5(a), during lithiation, Li covered the top surface of the circular Sn foil that contacted with electrolyte first and then flowed into the foil along the thickness direction. With Li insertion, a highly incompatible strain was generated at the reaction front, which, on the one hand, could lead to the expansion of the lithiated phase upward. For the same lithiation thickness, the volume expansion of the pristine Sn foil was much larger than that of the 3DIP-Sn foil, indicating that the porosity could effectively mitigate the Li insertion-induced volume strain. On the other hand, excessive stress both at and closely behind the reaction front was caused in the foils (Fig. 5b). Even though Li insertion-induced stress in the foil far away from the reaction front could be alleviated by the creep behavior of Sn and Li_xSn phases, the level of stress near the reaction front was too high to be relaxed in the pristine Sn foil. In contrast, the creep behavior of the 3DIP-Sn foil was highly promoted by the interconnected network structure, leading to the fast relaxation of the generated stress. During delithiation process, the Li extraction-induced stress could also be effectively alleviated by the interconnected porous structure, resulting in the recovery of the 3DIP-Sn foil to its original shape after full delithiation. Therefore, the 3DIP-Sn foil always suffered much less volume change and stress than the pristine Sn foil, contributing to the promoted electrochemical performance of the 3DIP-Sn foil observed in our experiments.

Moreover, full cells were fabricated using $LiFePO_4$ and $LiNi_{0.6}Co_{0.2}Mn_{0.2}O_2$ (NCM622) as the respective counter electrode to further explore the electrochemical performance of the 3DIP-Sn foil electrode. The Cyclic Voltammetry (CV) curves of 3DIP-Sn||$LiFePO_4$ and pristine Sn||$LiFePO_4$ cells were recorded at a scanning rate of 0.1 mV s^{-1} in the voltage range of 2.0–3.7 V (Figs. S13 and S14). The 3DIP-Sn||$LiFePO_4$ cell presented a single oxidation peak at 2.66 V and a reduction peak at 2.92 V, while pristine Sn||$LiFePO_4$ cell showed two redox peaks, which was in good agreement with the charge/discharge curves of the Sn||Li half cells. The evolutions of capacity and Coulombic efficiency (CE) of the cells with $LiFePO_4$ loadings of 1.8 and 7.1 mg cm^{-2} are shown in Fig. 6(a and b). Due to the unstable electrochemical property, the pristine Sn||$LiFePO_4$ cells showed varying capacities during the cycling, with the capacity increased first due to the activation process of pristine Sn foil and then decayed rapidly owing to the chemo-mechanical failure of the electrodes. As displayed in Fig. 6(a), the capacity of the pristine Sn||$LiFePO_4$ cell was 99.1 mAh g^{-1} initially, and it increased to 129.7 mAh g^{-1} after 60 cycles and then decayed to 70.5 mAh g^{-1} after 300 cycles 1C (1.4 mg cm^{-2}, 1C = 170 mA g^{-1}). In contrast, the 3DIP-Sn||$LiFePO_4$ cell exhibited a much higher initial specific capacity of 137.6 mAh g^{-1} and an initial CE of 87.4%. After running for 500 cycles at 1C (1.8 mg cm^{-2}, 1C = 170 mA g^{-1}), 80% capacity was still retained, indicating the excellent cyclability of the cell. When the mass loading of $LiFePO_4$ increased to 7.1 mg cm^{-2}, the 3DIP-Sn||$LiFePO_4$ cell also showed good cycle stability with a high-capacity retention of 80% after 500 cycles at 70 mA g^{-1} (Fig. 6b). Such improved electrochemical performance of the 3DIP-Sn electrode can be attributed to the elaborately designed 3D interconnected porous structure with highly refined grain size, which can effectively buffer volume change and mitigate the localized stress and subsequent damage that suffered by the pristine Sn electrode during Li insertion /extraction. More impressively, when pairing 3DIP-Sn foil against NCM622 cathode with ~ 18.4 mg cm^{-2} active material loading for higher full-cell voltage output (Fig. S15), the 3DIP-Sn||NCM622 cells delivered a high initial areal capacity of ~ 3.2 mAh cm^{-2} at 35 mA g^{-1}, and a reversible capacity of ~ 2.3 mAh cm^{-2} was well maintained after 100 cycles at 70 mA g^{-1} (Fig. 6c), demonstrating the potential capability of the 3DIP-Sn foil electrode for practical application.

In addition, the 3DIP-Sn||$LiFePO_4$ full cell exhibited outstanding rate capability in comparison to the pristine Sn||$LiFePO_4$ cell. The capacities of 3DIP-Sn||$LiFePO_4$ cell were 140.9, 136.4, 130.0, 120.3, 100.3, and 80.0 mAh g^{-1} at the current rates of 0.2, 0.5, 1.0, 2.0, and 10.0C, respectively (Fig. 6d). As shown in Fig. 6(e) and S16, the 3DIP-Sn||$LiFePO_4$ cell displayed one charge/discharge plateaus while the pristine Sn||$LiFePO_4$ cell showed two voltage plateaus, consistent with the CV results in Figs. S13 and S14. Moreover, the 3DIP-Sn||$LiFePO_4$ cell delivered a lower overpotential

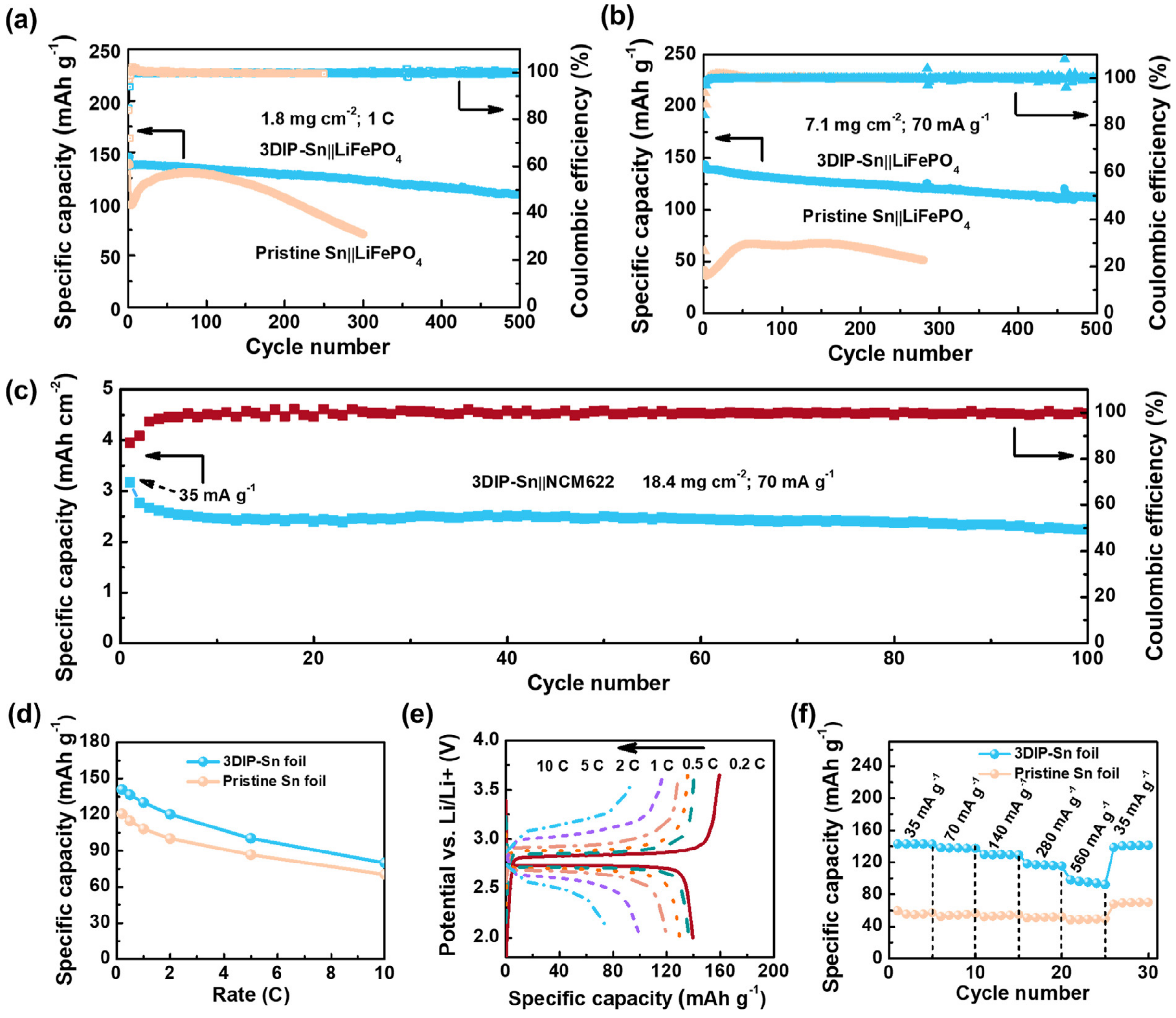

Fig. 6. Electrochemical cycling performance of the pristine Sn||$LiFePO_4$ and 3DIP-Sn||$LiFePO_4$ cells with $LiFePO_4$ loadings of (a) 1.7 mg cm^{-2} and (b) 7.1 mg cm^{-2}, respectively. (c) Cycling performance of the pristine Sn||NCM622 and 3DIP-Sn||NCM622 cells with NCM622 loading of ~ 18.4 mg cm^{-2}. (d) Rate capabilities of the pristine Sn||$LiFePO_4$ and 3DIPA-Sn||$LiFePO_4$ cells at various current densities with $LiFePO_4$ loading of ~ 1.7 mg cm^{-2}, and (e) the corresponding galvanostatic charge/discharge profiles for the 3DIP-Sn||$LiFePO_4$ cells. (f) Rate capabilities of the pristine Sn||$LiFePO_4$ and 3DIP-Sn||$LiFePO_4$ cells at various current densities with a $LiFePO_4$ loading of ~ 7.1 mg cm^{-2}.

than that of the pristine Sn||$LiFePO_4$ cell at various current densities. For example, the overpotential of 3DIP-Sn||$LiFePO_4$ cell was 0.11 V at 0.2C, lower than 0.36 V for the pristine Sn||$LiFePO_4$ cell. The rate performance of the 3DIP-Sn||$LiFePO_4$ cells was further studied with high $LiFePO_4$ mass loading of ~ 7.1 mg cm^{-2} (Fig. 6f), which delivered the specific capacities of 142.9, 138.0, 129.9, 118.2, and 98.3 mAh g^{-1} at the current densities of 35, 70, 140, 280, and 560 mA g^{-1}, respectively. When the current density was turned back to 35 mA g^{-1}, a high reversible capacity of 141.2 mAh g^{-1} was recovered. In contrast, only a low capacity of 70.1 mAh g^{-1} could be obtained for the pristine Sn||$LiFePO_4$ cell under the same test condition, demonstrating the outstanding rate capability and cycle performance of the 3DIP-Sn||$LiFePO_4$ cells with moderately high $LiFePO_4$ loading.

3. Conclusions

In summary, a 3DIP-Sn foil electrode was fabricated by a facile chemical alloying/dealloying approach. The 3D interconnected porous structure of the Sn foil could buffer the volume variation and improve the electrolyte wettability, and the refinement of grain size could eliminate the GB effects, and thus mitigate the stress localization during the lithiation/delithiation processes. Consequently, a long cycle lifespan of 4400 h was achieved for the 3DIP-Sn foil electrode in a half-cell configuration at 0.5 mA cm^{-2} and 1 mAh cm^{-2}. Pairing with $LiFePO_4$ cathode with a high active mass loading of ~ 7.1 mg cm^{-2}, the 3DIP-Sn||$LiFePO_4$ cell exhibited outstanding stable cycling with a high-capacity retention of 80% after 500 cycles at 70 mA g^{-1}. Moreover, the 3DIP-Sn||NCM622 full cell with cathode active mass loading of ~ 18.4 mg cm^{-2} displayed a high reversible capacity of 3.2 mAh cm^{-2}. This work sheds light on the important role of rational structure design in circumventing chemo-mechanical failure and enabling a stable high-capacity battery electrode for advanced LIBs.

Declaration of Competing Interest

The authors declare that they have no known competing financial interests or personal relationships that could have appeared to influence the work reported in this paper.

Acknowledgments

This work is financially supported by the National Natural Science Foundation of China (Grant Nos. 52072137, 51802105). The authors would also like to thank the Analytical and Testing

Center of Huazhong University of Science and Technology (HUST) as well as the Center for Nanoscale Characterization & Devices of Wuhan National Laboratory for Optoelectronics (WNLO) for providing the facilities to conduct the characterizations.

Appendix A. Supplementary data

Supplementary data to this article can be found online at https://doi.org/10.1016/j.jechem.2021.03.053.

References

[1] Y. Sun, N. Liu, Y. Cui, Nat. Energy 1 (2016) 16071.
[2] T. Chen, Y. Jin, H. Lv, A. Yang, M. Liu, B. Chen, Y. Xie, Q. Chen, Trans. Tianjin Univ. 26 (2020) 208–217.
[3] M. Li, J. Lu, Z. Chen, K. Amine, Adv. Mater. 30 (2018) 1800561.
[4] S. Tu, X. Chen, X. Zhao, M. Cheng, P. Xiong, Y. He, Q. Zhang, Y. Xu, Adv. Mater. 30 (2018) 1804581.
[5] Z. Liu, Q. Yu, Y. Zhao, R. He, M. Xu, S. Feng, S. Li, L. Zhou, L. Mai, Chem. Soc. Rev. 48 (2019) 285.
[6] Y. Zeng, Y. Huang, N. Liu, X. Wang, Y. Zhang, Y. Guo, H.-H. Wu, H. Chen, X. Tang, Q. Zhang, J. Energy Chem. 54 (2021) 727–735.
[7] G. Li, J.-Y. Li, F.-S. Yue, Q. Xu, T.-T. Zuo, Y.-X. Yin, Y.-G. Guo, Nano Energy 60 (2019) 485–492.
[8] B. Zhu, G. Liu, G. Lv, Y. Mu, Y. Zhao, Y. Wang, X. Li, P. Yao, Y. Deng, Y. Cui, J. Zhu, Sci. Adv. 5 (2019) eaax0651.
[9] W. Li, X. Sun, Y. Yu, Small Methods 1 (2017) 1600037.
[10] B.-Q. Xiong, X. Zhou, G.-L. Xu, X. Liu, Y. Hu, Y. Liu, L. Zhu, C.-G. Shi, Y.-H. Hong, S.-C. Wan, C.-J. Sun, S. Chen, L. Huang, S.-G. Sun, K. Amine, F.-S. Ke, ACS Energy Lett. 5 (2020) 3490–3497.
[11] X. Cao, Y. Fan, J. Qu, T. Wang, D. Legut, Q. Zhang, J. Energy Chem. 47 (2020) 160–165.
[12] X. Huang, S. Cui, J. Chang, P.B. Hallac, C.R. Fell, Y. Luo, B. Metz, J. Jiang, P.T. Hurley, J. Chen, Angew. Chem. 127 (2015) 1510–1513.
[13] H. Ying, W.-Q. Han, Adv. Sci. 4 (2017) 1700298.
[14] S. Lia, C. Wang, J. Yu, Y. Han, Z. Lu, Energy Storage Mater. 20 (2019) 7–13.
[15] M. Winter, J.O. Besenhard, Electrochim Acta 45 (1999) 31–50.
[16] N. Qaiser, Y.J. Kim, C.S. Hong, S.M. Han, J. Phys. Chem. C 120 (2016) 6953–6962.
[17] J.B. Cook, E. Detsi, Y. Liu, Y.-L. Liang, H.-S. Kim, X. Petrissans, B. Dunn, S.H. Tolbert, ACS Appl Mater. Interfaces 9 (2017) 293–303.
[18] Y. Xu, Q. Liu, Y. Zhu, Y. Liu, A. Langrock, M.R. Zachariah, C. Wang, Nano Lett. 13 (2013) 470–474.
[19] H. Shi, Z. Fang, X. Zhang, F. Li, Y. Tang, Y. Zhou, P. Wu, G. Yu, Nano Lett. 18 (2018) 3193–3198.
[20] J. Li, X. Xu, Z. Luo, C. Zhang, Y. Zuo, T. Zhang, P. Tang, M.F. Infante-Carrió, J. Arbiol, J. Llorca, J. Liu, A. Cabot, ChemSusChem 12 (2019) 145–1458.
[21] M.-G. Park, D.-H. Lee, H. Jung, J.-H. Choi, C.-M. Park, ACS Nano 12 (2018) 2955–2967.
[22] R.Z. Hu, Y. Zhang, M. Zhu, Electrochim Acta 53 (2008) 3377–3385.
[23] S. Yang, P.Y. Zavalij, M.S. Whittingham, Electrochem Commun. 5 (2003) 587–590.
[24] S.T. Boles, M.H. Tahmasebi, Joule 4 (2020) 1342–1346.
[25] M. Zhang, L. Xiang, M. Galluzzi, C. Jiang, S. Zhang, J. Li, Y. Tang, Adv. Mater. 31 (2019) 1900826.
[26] H. Fan, B. Chen, S. Li, Y. Yu, H. Xu, M. Jiang, Y. Huang, J. Li, Nano Lett. 20 (2020) 896–904.
[27] G. Wang, M. Aubin, A. Mehta, H. Tian, J. Chang, A. Kushima, Y. Sohn, Y. Yang, Adv. Mater. 32 (2020) 2003684.
[28] H. Xu, S. Li, X. Chen, C. Zhang, W. Liu, H. Fan, Y. Yu, Y. Huang, J. Li, Adv. Energy Mater. 9 (2019) 1902150.
[29] Q. Xiao, M. Gu, H. Yang, B. Li, C. Zhang, Y. Liu, F. Liu, F. Dai, L. Yang, Z. Liu, X. Xiao, G. Liu, P. Zhao, S. Zhang, C. Wang, Y. Lu, M. Cai, Nat Commun. 6 (2015) 8844.
[30] H. Yang, F. Fan, W. Liang, X. Guo, T. Zhu, S. Zhang, J. Mech. Phys. Solids 70 (2014) 349–361.
[31] H. Yang, S. Huang, X. Huang, F. Fan, W. Liang, X.H. Liu, L.-Q. Chen, J.Y. Huang, J. Li, T. Zhu, S. Zhang, Nano Lett. 12 (2012) 1953–1958.